

This is a repository copy of *Contrasting the Effects of Aspartic Acid and Glycine in Free Amino Acid and Peptide Forms on the Growth Rate, Morphology, Composition, and Structure of Synthetic Aragonites*.

White Rose Research Online URL for this paper:

<https://eprints.whiterose.ac.uk/219694/>

Version: Published Version

---

**Article:**

Gardella, Giacomo, Castillo Alvarez, Maria Cristina, Presslee, Sam et al. (5 more authors) (2024) *Contrasting the Effects of Aspartic Acid and Glycine in Free Amino Acid and Peptide Forms on the Growth Rate, Morphology, Composition, and Structure of Synthetic Aragonites*. *Crystal Growth and Design*. ISSN 1528-7483

<https://doi.org/10.1021/acs.cgd.4c00766>

---

**Reuse**

This article is distributed under the terms of the Creative Commons Attribution (CC BY) licence. This licence allows you to distribute, remix, tweak, and build upon the work, even commercially, as long as you credit the authors for the original work. More information and the full terms of the licence here:

<https://creativecommons.org/licenses/>

**Takedown**

If you consider content in White Rose Research Online to be in breach of UK law, please notify us by emailing [eprints@whiterose.ac.uk](mailto:eprints@whiterose.ac.uk) including the URL of the record and the reason for the withdrawal request.

# Contrasting the Effects of Aspartic Acid and Glycine in Free Amino Acid and Peptide Forms on the Growth Rate, Morphology, Composition, and Structure of Synthetic Aragonites

Giacomo Gardella, Maria Cristina Castillo Alvarez, Sam Presslee, Adrian A. Finch, Kirsty Penkman, Roland Kröger, Matthieu Clog, and Nicola Allison\*



Cite This: <https://doi.org/10.1021/acs.cgd.4c00766>



Read Online

ACCESS |



Metrics & More

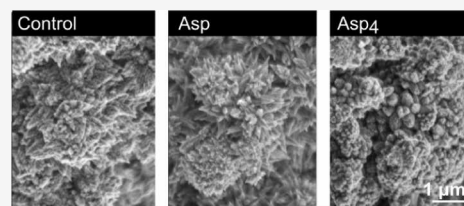


Article Recommendations



Supporting Information

**ABSTRACT:** Corals and mollusks produce aragonite skeletons and shells containing highly acidic proteins, rich in aspartic acid (Asp) and glycine (Gly). These biomolecules are pivotal in controlling biomineral formation. We explore the effects of *L*-Asp, Gly, and two peptides: glycyl-*L*-aspartic acid (Gly-Asp) and tetra-aspartic acid (Asp<sub>4</sub>) on the precipitation rate, crystal morphology, and CO<sub>3</sub> group rotational disorder (inferred from Raman spectroscopy) in aragonite precipitated *in vitro* at the approximate pH, [Ca<sup>2+</sup>], and Ω<sub>ar</sub> occurring in coral calcification media. All of the biomolecules, except Gly, inhibit aragonite precipitation. Biomolecules are incorporated into the aragonite and create CO<sub>3</sub> group rotational disorder in the following order: Asp<sub>4</sub> > Asp = Gly-Asp > Gly. Asp<sub>4</sub> inhibits aragonite precipitation more than Asp at comparable solution concentrations, but Asp reduces aragonite precipitation more effectively than Asp<sub>4</sub> for each Asp residue incorporated into the aragonite. At the highest solution concentration, the molar ratio of Asp<sub>4</sub>:CaCO<sub>3</sub> in the aragonite is 1:690. We observe a significant inverse relationship between the aragonite precipitation rate and aragonite Raman spectrum ν<sub>1</sub> peak fwhm across the entire data set. Tetra-aspartic acid inhibits aragonite precipitation at all concentrations, suggesting that the aspartic acid-rich domains of coral skeletal proteins influence biomineralization by suppressing mineral formation, thereby shaping skeletal morphology and preventing uncontrolled precipitation.



## 1. INTRODUCTION

Calcareous organisms produce CaCO<sub>3</sub> structures, which confer protection to the organisms, contribute to habitats, and influence the global carbon cycle. CaCO<sub>3</sub> biominerals are hierarchically structured, organic–inorganic composite minerals containing a variety of biomolecules.<sup>1,2</sup> Organisms secrete biomolecules to exert biological control over different stages of biomineralization, including nucleation, growth, and crystal morphology.<sup>2,3</sup> In addition, biomolecules confer different physical properties on biominerals compared to their fully inorganic counterparts.<sup>4,5</sup> This allows organisms to improve the mechanical properties (e.g., fracture resistance and hardness) of the biominerals compared to inorganic analogues.<sup>6</sup>

Identifying how biomolecules influence CaCO<sub>3</sub> formation is critical to understanding their role in biomineralization. CaCO<sub>3</sub> growth proceeds by the attachment of ions to the crystal surface, with a high probability of attachment at kink sites (disjoints on the crystal surface).<sup>7</sup> Growth may also reflect the attachment of nanocrystals<sup>8</sup> or amorphous calcium carbonates (ACCs) as reported in coral aragonite biomineralization.<sup>9</sup> Biomolecules/additives may affect CaCO<sub>3</sub> formation by binding the aqueous ions required for mineral formation, thereby altering their availability for precipitation, e.g., amino acids can complex Ca<sup>2+</sup> in seawater.<sup>10</sup> Additives

may also block attachment sites on the existing crystal surface<sup>7</sup> and alter the formation of CaCO<sub>3</sub> precursor phases.<sup>11–13</sup>

Amino acids can influence the formation and stability of CaCO<sub>3</sub> precursors<sup>14</sup> and alter the polymorph, crystal shape, and size of precipitated CaCO<sub>3</sub>.<sup>15</sup> Amino acids and peptides promote or inhibit CaCO<sub>3</sub> precipitation.<sup>16–18</sup> In the marine environment, multiple organisms produce aragonite, including polychaete worms,<sup>19</sup> some foraminifera,<sup>20</sup> mollusks,<sup>21</sup> and corals.<sup>22</sup> Despite this importance, relatively few studies have investigated the influence of biomolecules on aragonite crystallization.<sup>18,23,24</sup> Identifying the biomolecule role in aragonite formation is especially important as the total organic and amino acid concentration of tropical coral skeletons is increased in specimens cultured under future ocean acidification scenarios.<sup>24–26</sup> Resolving how biomolecules affect aragonite formation is important in predicting the future accretion rates and structural resilience of coral reefs.

**Received:** June 5, 2024

**Revised:** October 24, 2024

**Accepted:** October 25, 2024

In this study, we explore the effects of two free amino acids and two peptides on the precipitation rate, morphology, and  $\text{CO}_3$  group disorder in the crystal lattice of aragonite. Aspartic acid (termed Asp) is an important component of biomineralization proteins in mollusk shells<sup>27–29</sup> and coral skeletons.<sup>1,24,30</sup> Glycine (termed Gly) also occurs in high concentrations in coral skeletons<sup>1,24</sup> and mollusk nacre.<sup>28</sup> Asp is an acidic amino acid with a  $\text{COOH}$  side chain, which is deprotonated (to  $\text{COO}^-$ ) at physiological pH to produce the anion aspartate. Gly is a neutral amino acid, zwitterionic, but overall uncharged at physiological pH.<sup>31</sup> Both amino acids complex  $\text{Ca}^{2+}$  in solution<sup>10,32</sup> and adsorb to calcite crystal faces.<sup>17</sup> We also explore the effects of the dipeptide glycyl-L-aspartic acid (termed Gly-Asp) and the tetra peptide tetra-aspartic acid (termed Asp<sub>4</sub>). Aspartic acid-rich domains are common in biomineralization proteins<sup>30</sup> and contrasting the effects of peptides and free amino acids provides information on the role of molecule size in interactions with  $\text{CaCO}_3$  (Figure 1).

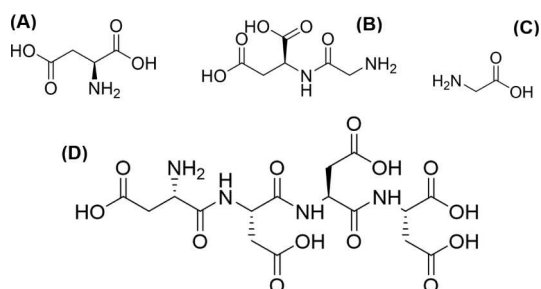


**Figure 1.** Biomolecules used in this study (A) Asp, (B) Gly-Asp, (C) Gly, and (D) Asp<sub>4</sub>.

For this study, we precipitated aragonite in vitro from modified seawater at the pH and saturation state ( $\Omega_{\text{ar}}$ ) believed to occur at the calcification site of tropical corals. We used an apparatus designed to maintain the pH and content of the solution at a constant composition.<sup>18</sup> We determine aragonite precipitation rates in the presence and absence of biomolecules, measure biomolecule incorporation in aragonite by reverse phase high-performance liquid chromatography (RP-HPLC), and explore how biomolecules alter aragonite morphology. Finally, we analyze the precipitates by Raman spectroscopy. The most prominent band in the aragonite Raman spectrum, the  $\nu_1$  band, reflects symmetric C–O stretching in the planar  $\text{CO}_3$  group. An increase in its full width at half-maximum (fwhm, a metric of the peak breadth normalized for peak height) is linked to increased local disorder around this group in the  $\text{CaCO}_3$  lattice.<sup>33,34</sup> We therefore explore how aragonite formation in the presence of biomolecules affects this disorder.

## 2. METHODS

**2.1. Aragonite Precipitation Experiments.** Synthetic aragonites were precipitated using the constant composition technique<sup>35</sup> using a Metrohm Titrando 902 pH stat titrator. This method relies on the addition of equal volumes of  $\text{CaCl}_2$  and  $\text{Na}_2\text{CO}_3$  to maintain constant pH and  $\Omega$ , while  $\text{CaCO}_3$  precipitates. For further details of the apparatus used here, see refs<sup>18,23</sup>. The titrants used were 0.4455 M  $\text{CaCl}_2$  + 0.0045 M  $\text{SrCl}_2$  and 0.45 M  $\text{Na}_2\text{CO}_3$ . Sr was replenished in the reaction vessel as it substitutes for  $\text{Ca}^{2+}$  ions in aragonite.<sup>36</sup> Titrants

were added automatically, when the pH of the solution, which decreases due to the precipitation of calcium carbonate, fell below 0.003 pH units of the set value. The standard deviation of pH measurements measured every 1 to 5 s during each titration was <0.005 pH units, and we considered the pH of the solution to be essentially constant. An aragonite seed was added to provide a surface for aragonite growth. For all experiments reported here, aragonite was precipitated from artificial seawater (to the composition of Millero<sup>37</sup> and with  $S = 35$ ), filtered with a 0.2  $\mu\text{m}$  polycarbonate filter, and stored in 100 L blacked-out HDPE tanks. Prior to use, the seawater was bubbled with atmospheric air sourced from outside the building ( $\sim 416$  ppm of  $p\text{CO}_2$ ) and then adjusted to  $\text{pH}_{\text{NBS}} = 8.445$  and dissolved inorganic carbon concentration ( $[\text{DIC}] = 4000 \mu\text{mol kg}^{-1}$ ) by the addition of 0.6 M  $\text{Na}_2\text{CO}_3$  (to increase DIC) and 2 M HCl or NaOH (to control pH). We estimate solution  $\Omega_{\text{aragonite}} = 11.4$  using  $\text{CO}_2\text{SYS v2.1}$ <sup>38</sup> with the equilibrium constants for carbonic acid<sup>39</sup> and  $\text{KHSO}_4$ <sup>40</sup> and using  $[\text{B}]_{\text{seawater}}$ <sup>41</sup>

Where used, biomolecules were dissolved in aliquots of this manipulated seawater and added to the reaction vessel shortly before the start of the experiment, allowing time for final pH adjustments. All biomolecules were sourced from Sigma-Aldrich and had a purity of >97% for Asp<sub>4</sub> and >99% for all others. pH was monitored using a combined pH electrode and temperature sensor (Metrohm Aquatrode PT1000). The apparatus was cleaned with 0.1 M HCl, and the titrant dosing tubes were submerged in 1 M HCl between experiments.

In the first series of experiments, reactions were conducted with either a) no biomolecule (control), b) 2 mM L-Asp, c) 2 mM Gly, d) 2 mM Gly-Asp dipeptide, or e) 2 mM Asp + 2 mM Gly (both amino acids added separately). Precipitations were conducted in 330 mL of seawater contained in a high density polyethylene (HDPE) beaker maintained in a water bath at 25 °C. The beaker was capped with an ethylene tetrafluoroethylene lid with ports to insert the following: a pH/temperature sensor, a propeller stirrer, a gas tube (supplying air with  $\sim 416$  ppm  $p\text{CO}_2$  into the headspace), and the two titrant dosing tubes. For each experiment, the seed consisted of  $200 \pm 2$  mg of a *Porites lutea* skeleton, which was wet ground using an agate ball mill to produce a powder with a surface area of  $4.70 \pm 0.14 \text{ m}^2 \text{ g}^{-1}$  (mean  $\pm 1$  standard deviation,  $n = 3$ ) as determined by the Brunauer–Emmett–Teller technique.<sup>42</sup> The seed was suspended in 1 mL of the seawater solution, agitated on a vortex mixer, and added to the reaction vessel at the start of the experiment. The experiment proceeded until 7 mL of each titrant was dosed, resulting in the precipitation of  $\sim 315$  mg of aragonite in vitro. 5–7 replicates of each treatment were conducted. Over the course of the precipitation, solution temperature varied by <0.5 °C and is considered essentially constant.

The  $[\text{DIC}]$  of the reaction solution was measured before the seed was added and just before the end of the experiment using an Apollo Sci Tech AS-C3 DIC<sup>43</sup> for a subset ( $n = 24$ ) of the precipitation experiments. For this, 12 mL of the experiment solution was filtered through a 0.22  $\mu\text{m}$  polyether sulfone syringe filter, and 0.6 mL was injected into the analyzer. The measurement was replicated 5 times after flushing with the filtrate. The DIC analyzer was calibrated before every session with a seawater certified reference material (Dickson batch 171). The difference between measured  $[\text{DIC}]$  and expected  $[\text{DIC}]$  was <50  $\mu\text{mol kg}^{-1}$  for controls and <65  $\mu\text{mol kg}^{-1}$  for all other experiments, and the difference between  $[\text{DIC}]$  at the

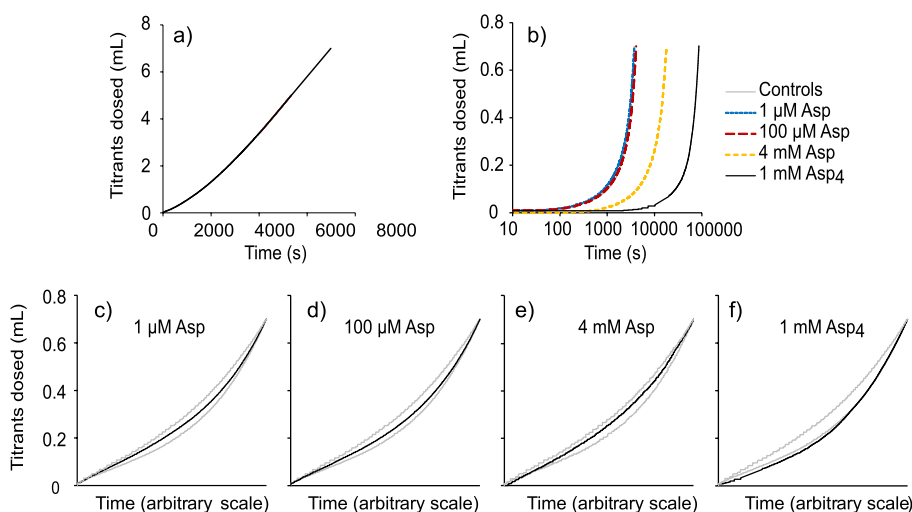


**Figure 2.** Profiles showing titrant dosing as a function of time in a) a control experiment in 330 mL of solution and b) control, Asp, and Asp<sub>4</sub> titrations in a 33 mL solution (note the log *x*-axis). c–f) Profiles for 33 mL experiments were scaled so that the maximum titrant volume dosed occurs at the limit of the *x* axis (linear scale). Profiles for two control (no biomolecule) experiments are superimposed on each graph in gray for comparison.

start and end of the precipitation was 4% on average and always <8%. These minor variations in [DIC] indicate that CO<sub>2</sub> invasion or outgassing during the experiments was minimal (see the Method section in the [Supporting Information](#)). The average change in [DIC] of 4% over a titration is equivalent to a change in  $\Omega_{\text{aragonite}}$  of 0.4.

In the second set of experiments, aragonite was precipitated in the presence of varying concentrations (1–4000  $\mu\text{M}$ ) of Asp and Asp<sub>4</sub>. Due to the limited availability of the peptide, these precipitations were conducted in a smaller HDPE beaker filled with 33 mL of artificial seawater. No lid was used, and the pH sensor and titrant tubes were inserted through the top of the beaker. The seed was 20 mg of synthetic aragonite precipitated at  $\Omega_{\text{aragonite}} = 11$  using the same pH stat titrator utilized in this study and wet ground to yield a surface area of 5.13 m<sup>2</sup> g<sup>-1</sup> as determined by the Brunauer–Emmett–Teller technique.<sup>39</sup> 0.7 mL of each titrant was added to the solution, resulting in the precipitation of ~32 mg of aragonite. The reaction vessel was kept in a controlled temperature room maintained at 25 °C and was stirred using an 8 mm length magnetic stirrer on a stirrer plate. Over the course of the precipitation, the solution temperature varied by up to 1 °C. The reaction vessel was too small to permit DIC analyses at the start and end of precipitations, but solutions set up using the same method had [DIC] of 3950–4100  $\mu\text{mol kg}^{-1}$ . 2–3 replicates were conducted for each treatment, with the exception of the experiment with 1000  $\mu\text{M}$  Asp<sub>4</sub>, which was only conducted once, as this final experiment took more than 24 h.

For both series of experiments, the solids (original seed plus precipitate) were recovered by filtering the reaction solution through a 0.2  $\mu\text{m}$  polycarbonate filter (Nucleopore), rinsing with deionized water (18.2 Megaohm) and ethanol, drying at room temperature, and then storing in a desiccator.

In the 330 mL experiments, the rate of titrant dosing was approximately constant, resulting in a linear relationship between the time and the volume of titrant dosed (Figure 2a). Such a profile is generated when aragonite precipitation has little effect on the surface area for subsequent aragonite growth during the titration.<sup>18</sup> In these experiments, the aragonite precipitation rate is calculated from the rate of

titrant addition (to replace the CO<sub>3</sub><sup>2-</sup> and Ca<sup>2+</sup> consumed during CaCO<sub>3</sub> formation) normalized to the surface area of the seed.<sup>18</sup> We test for differences in the aragonite precipitation rate between treatments using one-way ANOVA followed by Tukey's pairwise comparison.

In the 33 mL experiments, the rates of titrant dosing accelerated as the experiment progressed (Figure 2b). This occurs as precipitation increases the surface area for aragonite growth during the experiment.<sup>18</sup> The seed surface area to solution volume ratio was the same in the 330 and 33 mL experiments. However, nucleation of minor amounts of CaCO<sub>3</sub> on the glass pH sensor or the titrant dosing tubes could increase the surface area for aragonite growth in the 33 mL experiments while having a negligible effect in the 330 mL experiments. We plot the titration profiles for 33 mL control experiments and those with varying concentrations of Asp and Asp<sub>4</sub> so that the profiles can be directly superimposed (Figure 2 c–f). These plots demonstrate that the titrant dosing profile does not vary in shape between treatments. This confirms that although the surface area for aragonite growth increases in 33 mL, it does so in a similar manner in all the treatments; i.e., although the aragonite precipitation rate is usually slower with biomolecules (Figure 2b), the surface area for aragonite growth appears to increase in a similar manner (albeit over a different time scale) between treatments. We infer that the surface area for aragonite growth is the same in all the 33 mL experiments, and we use the total time to dose 0.7 mL of titrant to estimate the aragonite precipitation rate, assuming that the mean dosing time of 3738 s observed in the control titrations reflects a precipitation rate of 2011  $\mu\text{mol m}^2 \text{h}^{-1}$  (as observed in a 330 mL experiment with the same seed) and scaling dosing time to precipitation rate in a linear manner. By this method, we estimate a mean aragonite precipitation rate of 1442  $\mu\text{mol m}^2 \text{h}^{-1}$  in the treatment with 1 mM Asp, which is in reasonable agreement with a previously reported rate (1106  $\mu\text{mol m}^2 \text{h}^{-1}$ ).<sup>18</sup>

**2.2. Amino Acid Analysis.** The [Asp] and [Gly] of the intracrystalline fraction of the aragonite precipitates were determined by reverse-phase HPLC with fluorescence detection, following the method of Hendy et al.<sup>44</sup> (a

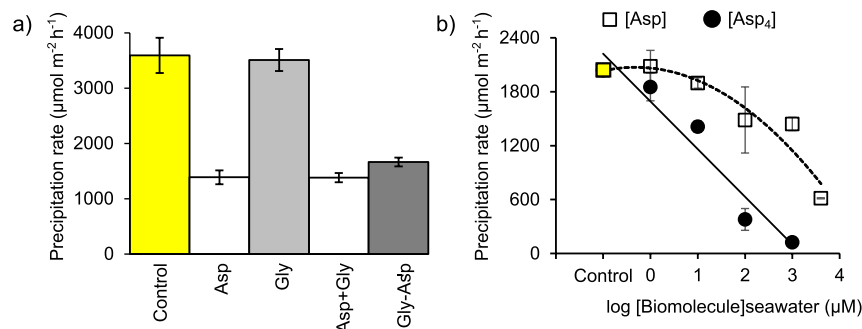


**Figure 3.** Aragonite precipitation rates in seawater at  $\Omega_{\text{aragonite}} = 11$  in a) 330 mL experiments with 2 mM biomolecules, where used, and b) 33 mL experiments at varying concentrations of Asp or Asp<sub>4</sub>. Lines indicate best-fit relationships between seawater [biomolecule] and the precipitation rate in b). Error bars are standard deviations of 5–7 replicates in a) and 2–3 replicates (except for 1000  $\mu\text{M}$  Asp<sub>4</sub>, where  $n = 1$ ) in b). In b), many error bars are smaller than the symbols.

modification of Kaufman and Manley).<sup>45</sup> <20 mg of aragonite was accurately weighed into a plastic microcentrifuge tube, bleached using 50  $\mu\text{L}$  of 12% NaOCl per mg for 48 h (to oxidize any surficial amino acids), then sequentially rinsed with 18.2 M  $\Omega$  H<sub>2</sub>O and methanol, and dried overnight. Samples precipitated with peptides were run as both free and hydrolyzed samples to determine if amino acids were incorporated in the peptide form (and therefore detectable in hydrolyzed samples only) or as free amino acids (i.e., after hydrolysis of the peptide in seawater during the titration or during precipitation). Samples precipitated in the presence of free amino acids were typically not hydrolyzed before analysis, but demineralized in 2 M HCl (10  $\mu\text{L}/\text{mg}$ ) and spun to dryness in a centrifugal evaporator. To hydrolyze the peptide bonds in the samples, <10 mg was accurately weighed into a 2 mL sterile glass vial (Wheaton) and 20  $\mu\text{L}/\text{mg}$  7 M HCl was added. After a flush with nitrogen, the vials were heated at 110  $^{\circ}\text{C}$  for 24 h. Upon removal, samples were dried in a centrifugal evaporator overnight. Both the free and hydrolyzed samples were rehydrated in a solution containing 0.01 mM L-homoarginine (as an internal standard) and analyzed using an Agilent 1100 HPLC with a fluorescence detector. 2  $\mu\text{L}$  of sample was injected and mixed for 13 cycles with 2.2  $\mu\text{L}$  of a derivatizing reagent (260 mM *n*-iso-L-butryl L-cysteine (IBLC) and 170 mM *o*-phthalaldehyde (OPA) in 1 M potassium borate buffer). The amino acids were separated on a C18 HyperSil BDS column (3  $\times$  250 mm) at 25  $^{\circ}\text{C}$  using a gradient elution of three solvents (Table S1: sodium acetate buffer (solvent A; 23 mM sodium acetate trihydrate, 1.5 mM sodium azide, 1.3  $\mu\text{M}$  EDTA, adjusted to pH 6.00  $\pm$  0.01 with 10% acetic acid and 10 M sodium hydroxide), methanol (solvent C), and acetonitrile (solvent D)), at an initial flow rate of 0.56 mL/min increasing to 0.6 mL/min, and a 95 min cutoff. The final [amino acid] of the aragonite precipitated in vitro was calculated by correcting the [amino acid] of the final sample for the [amino acid] of the seed.

**2.3. Raman Spectroscopy.** Raman spectra were collected from the starting seeds and at least two replicate titrations of each treatment, except for the Asp<sub>4</sub> treatment, which had no replicate. Spectra were collected using a Renishaw In-Via Qontor Raman microscope using a NIR 300 mW 785 nm solid-state laser set at 5% full power with a 1200 1/mm grating at a spectral resolution of 1  $\text{cm}^{-1}$ . The instrument was calibrated using the 520  $\text{cm}^{-1}$  vibrational model of a Si standard. For each analysis (spectrum), the laser was focused onto the edge of particles, and the spectrum was collected

between 100 and 1311  $\text{cm}^{-1}$  for 2 s in each acquisition, with the cosmic ray removal function enabled, and 10 acquisitions were summed to give a final spectrum. Spectra were collected from 10 to 25 particles in each aragonite sample. The full width at half-maximum (fwhm) of the  $\nu_1$  peak was estimated by fitting the  $\nu_1$  peak between 1060 and 1120  $\text{cm}^{-1}$  with a Voigt fit using the software Origin 2021 (OriginLab Corporation). Measured fwhm was corrected to true fwhm using the instrument spectral resolution.<sup>46</sup>

We also collected spectra for solid Gly, Asp, and Gly-Asp. These biomolecules exhibit multiple Raman bands between 120 and 1120  $\text{cm}^{-1}$  (Figure S1), but the most intense bands for each biomolecule (i.e., at 893  $\text{cm}^{-1}$  for Gly, at 940  $\text{cm}^{-1}$  for Asp, and at 935  $\text{cm}^{-1}$  for Gly-Asp) were not observed in the aragonite spectra, confirming that the biomolecule spectra do not affect the  $\nu_1$ -CO<sub>3</sub> vibrational mode fwhm. The Raman spectrum of aqueous glycine is pH dependent<sup>47</sup> but changes are minor and no Raman bands are observed at  $\sim$ 1083  $\text{cm}^{-1}$  that could interfere with the aragonite  $\nu_1$  peak fwhm. Finally, we confirmed that the fwhm of the  $\nu_1$  peak was not affected during analysis by collecting 12 spectra (120 acquisitions) on the same locations of particles precipitated with no biomolecule and with 1 mM Asp<sub>4</sub> or 8.7 mM Asp (Figure S2).

We collected 50 spectra from three of the control precipitates and confirmed that the fwhm population was normally distributed (Shapiro–Wilk test,  $p = 0.93$ ). We assume normal distributions for the other treatments, combine all fwhm data from replicates of the same treatment, and test for differences in the fwhm between treatments using one-way ANOVA followed by Tukey’s pairwise comparison.

**2.4. Scanning Electron Microscopy.** Scanning electron microscopy (SEM) images were collected for selected aragonite samples. Precipitates were mounted on aluminum pin stubs using double-sided carbon adhesive discs and viewed uncoated in a JEOL 7800F Prime (at the Nanocenter, University of York), using an accelerating voltage of 2.0 keV and a working distance of 10 mm.

### 3. RESULTS

All data (precipitation rates, aragonite [amino acid], and Raman  $\nu_1$  band fwhm) are included in Tables S2–S6. All precipitates exhibit Raman lattice mode peaks at  $\sim$ 153 and 206  $\text{cm}^{-1}$  and a dual peak ( $\nu_4$ ) between 700 and 710  $\text{cm}^{-1}$ , indicating that all samples consist essentially of aragonite.<sup>48,49</sup>

**3.1. Influence of Biomolecules on Aragonite Precipitation.** Aragonite precipitation rate is significantly lower in

Table 1. Summary of *p*-Values Generated in the ANOVA Analyses in this Study<sup>ab</sup>

ANOVA to Compare Aragonite Precipitation Rates between 330 mL Experiments (Figure 3a)					
	Asp	Gly	Gly-Asp	Gly + Asp	
control	<b><math>3.5 \times 10^{-14}</math></b>	0.93	<b><math>7.9 \times 10^{-14}</math></b>	<b><math>3.3 \times 10^{-14}</math></b>	
Asp	—	<b><math>3.8 \times 10^{-14}</math></b>	0.21	1.00	
Gly	—	—	<b><math>1.6 \times 10^{-13}</math></b>	<b><math>3.4 \times 10^{-14}</math></b>	
Gly-Asp	—	—	—	0.16	
ANOVA to Compare Raman $\nu_1$ fwhm between 330 mL Experiments (Figure 4a)					
	Asp	Gly	Gly-Asp	Gly + Asp	
control	<b><math>6.5 \times 10^{-12}</math></b>	0.35	<b><math>8.0 \times 10^{-10}</math></b>	<b><math>&lt;1 \times 10^{-21}</math></b>	
Asp	—	<b><math>3.6 \times 10^{-7}</math></b>	0.92	<b>0.0066</b>	
Gly	—	—	<b><math>1.8 \times 10^{-5}</math></b>	<b><math>2.5 \times 10^{-14}</math></b>	
Gly-Asp	—	—	—	<b>0.00021</b>	
ANOVA to Compare Raman $\nu_1$ fwhm between 33 mL Experiments (Figure 4b)					
	1 $\mu$ M Asp	10 $\mu$ M Asp	100 $\mu$ M Asp	1 mM Asp	4 mM Asp
control	0.97	<b><math>3.3 \times 10^{-5}</math></b>	<b><math>3.2 \times 10^{-9}</math></b>	<b><math>2.0 \times 10^{-3}</math></b>	<b><math>5.0 \times 10^{-6}</math></b>
	1 $\mu$ M Asp <sub>4</sub>	10 $\mu$ M Asp <sub>4</sub>	100 $\mu$ M Asp <sub>4</sub>	1 mM Asp <sub>4</sub>	1 mM Asp <sub>4</sub>
control	<b><math>8.4 \times 10^{-3}</math></b>	0.80	<b><math>1.7 \times 10^{-5}</math></b>	<b><math>1.7 \times 10^{-5}</math></b>	<b><math>1.9 \times 10^{-3}</math></b>
4 mM Asp					<b><math>1.9 \times 10^{-3}</math></b>

<sup>a</sup>We use one-way ANOVA and Tukey's HSD to compare aragonite precipitation rates and Raman spectra  $\nu_1$  FWHM between treatments with and without 2 mM biomolecules. <sup>b</sup>*p*-values  $\leq 0.05$  are highlighted in bold.

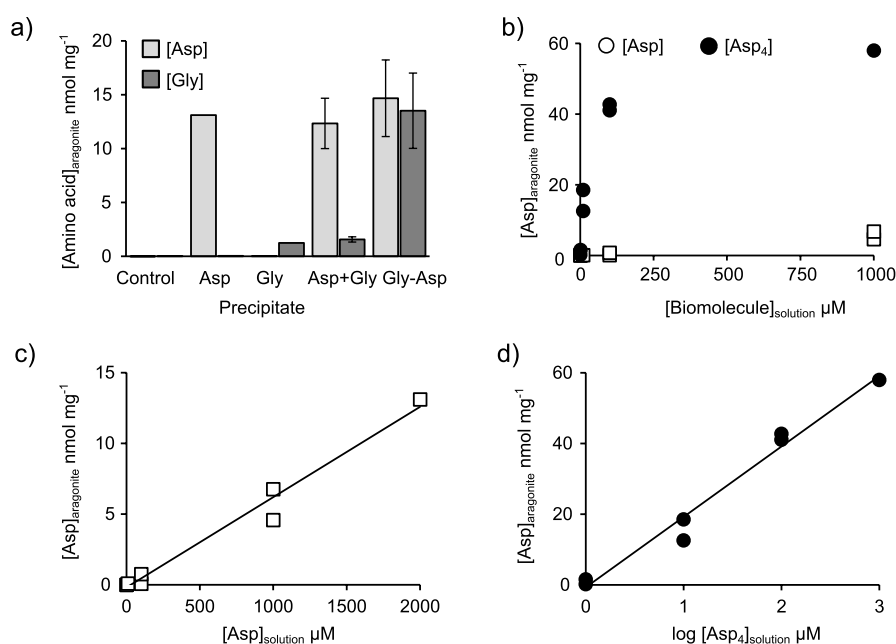


**Figure 4.** [Amino acid] in synthetic aragonite precipitated in vitro. Concentrations in a) aragonite precipitated in the presence of 2 mM of free amino acids, of the dipeptide Gly-Asp and in the presence of 2 mM Asp + 2 mM Gly (Asp+Gly) in combination, in the 330 mL experiments, and b) aragonite precipitated over variable concentrations of Asp and Asp<sub>4</sub> in the 33 mL experiments. c) A linear plot for the Asp data including both 330 and 33 mL experiments, and d) a log plot for the Asp<sub>4</sub> data. Seawater [biomolecule] indicates the concentration at the start of the experiment. In a), error bars indicate the standard deviation of duplicate analyses of repeat precipitations. In b–d, duplicate analyses are shown as separate points.

the presence of 2 mM Asp, Asp+Gly, and Gly-Asp compared with the control (Figure 3 and Table 1). 2 mM Gly has no significant effect on the aragonite precipitation rate compared to the control, and neither Gly-Asp nor Asp+Gly results in a significant change to the aragonite precipitation rate compared to Asp in isolation.

Asp<sub>4</sub> inhibits the aragonite precipitation rate at all the concentrations tested, with inhibition increasing from 9% at 1  $\mu$ M to 94% at 1000  $\mu$ M (Figure 3b). Asp marginally increases the aragonite precipitation rate at 1  $\mu$ M and then progressively

inhibits precipitation at higher concentrations. Asp<sub>4</sub> slows aragonite precipitation to a much greater degree than Asp, even when the number of aspartic acid residues in solution is considered (Figure 3b).

**3.2. Amino Acid Incorporation into Aragonite.** [Asp] and [Gly] in aragonite precipitated with no added amino acids are both 0 pmol mg<sup>-1</sup> in experiments analyzed for free amino acids and <212 and <156 pmol mg<sup>-1</sup> respectively, for hydrolyzed samples (Table S4). These values are <2% of the maximum concentrations observed in the aragonite samples

precipitated with biomolecules and are considered insignificant. In the case of aragonite precipitated with peptide, free amino acids contribute <2% of the total precipitate [amino acid] (Table S4), indicating that the amino acids detected in the aragonite are incorporated predominantly in their peptide form.

Asp and Gly are incorporated into aragonite precipitated in the presence of free forms of these amino acids (Figure 4). Asp is incorporated at more than 10 times the concentration of Gly from solutions of each amino acid at 2 mM, i.e., 13 nmol mg<sup>-1</sup> for Asp versus 1.3 nmol mg<sup>-1</sup> for Gly (Figure 4a). Both Asp and Gly are incorporated at similar concentrations in aragonite precipitated with the dipeptide Asp-Gly at 2 mM i.e., 14.7 nmol mg<sup>-1</sup> for Asp versus 13.5 nmol mg<sup>-1</sup> for Gly. When the two amino acids are simply put together in solution in their free forms (Asp+Gly), the amino acids are incorporated at similar concentrations to those observed when aragonite is precipitated with Asp or Gly only, i.e., Asp is preferentially incorporated into the precipitate (Figure 4a). Asp incorporation into aragonite increases as a function of seawater [Asp] and [Asp<sub>4</sub>] (Figure 4b). This relationship is linear in the experiments with [Asp] ranging from 0 to 2 mM (the maximum in our experiments; Figure 4c). Incorporation of Asp plateaus at higher concentrations in the Asp<sub>4</sub> experiments (Figure 4b), and incorporation in these experiments is best fit with a plot of log[Asp]<sub>solution</sub> versus [Asp]<sub>aragonite</sub> (Figure 4d).

32 and 315 mg of aragonite were precipitated in the 33 and 330 mL experiments, respectively. We calculate the seawater [biomolecule] at the end of the precipitations, assuming that any biomolecule not incorporated in the aragonite remains in solution and that the incorporation of 1 nmol Asp<sub>4</sub> increases aragonite [Asp] by 4 nmol (reflecting the number of residues in the peptide). In the free Asp experiments, <1% of the dissolved Asp is incorporated into the aragonite. However, approximately one-third of the Asp<sub>4</sub> dissolved into seawater at the start of the titrations is incorporated into the aragonite at starting [seawater Asp<sub>4</sub>] of 1 and 10 μM, and about 10% is incorporated at [seawater Asp<sub>4</sub>] of 100 μM.

**3.3. Biomolecules and Raman Aragonite Spectrum  $\nu_1$  Fwhm.** The Raman  $\nu_1$  fwhm increases significantly in synthetic aragonite precipitated with 2 mM Asp, 2 mM Gly-Asp, and 2 mM Asp + 2 mM Gly compared to the control (Table 1 and Figure 5a). 2 mM Gly does not significantly affect

the fwhm. The aragonite precipitated with 2 mM Asp + 2 mM Gly has a significantly broader fwhm than aragonite precipitated with 2 mM Asp only (Table 1).

The  $\nu_1$  fwhm decreases significantly with 10 and 100 μM Asp but increases significantly with 1 and 4 mM Asp compared to the control (Table 1 and Figure 5b). Asp<sub>4</sub> significantly increases the fwhm at 1, 100, and 1000 μM, but not at 10 μM (Table 1). The fwhm is significantly broader with 1 mM Asp<sub>4</sub> compared to 4 mM Asp (Figure 5b and Table 1).

We plot the change in fwhm ( $\Delta$ fwhm i.e., the increase/decrease in fwhm compared to the relevant control) as a function of aragonite [Asp] (Figure 6a) and the aragonite precipitation rate (Figure 6b).  $\Delta$ fwhm is significantly related to aragonite precipitation in the Asp<sub>4</sub> data set and when both Asp and Asp<sub>4</sub> precipitations are combined, but all other relationships between  $\Delta$ fwhm and seawater or aragonite biomolecule concentrations or the precipitation rate are insignificant (Table 2).

**3.4. Aragonite Morphology.** In all of the aragonite precipitated in the 330 mL experiments, the surface morphology is dominated by pyramidal clusters with crystals radiating in different directions from a common point (Figure 7). Differences in morphology between treatments are subtle, but aragonite crystals produced in the presence of 2 mM Gly are blunter than those observed in the controls (Figure 7b and d), while aragonite crystals produced with 2 mM Asp, Gly-Asp, and 2 mM Asp + 2 mM Gly are spikier, with narrower tips than in the control (Figure 7c,e, and f). Similar clusters of aragonite crystals are observed in the 33 mL experiments (Figure 8), but in this case, the effects of the biomolecules are more pronounced. High concentrations of Asp (1000 and 4000 μM) generate pointier, spikier crystals than in the control (Figure 8a, f and h), while 100 and 1000 μM Asp<sub>4</sub> results in blunt, rounder crystals (Figure 8e,g). Lower magnification images of all precipitates are included in the Figures S4 and S5.

## 4. DISCUSSION

**4.1. Biomolecules and Aragonite Precipitation.** In the aragonite precipitated in the presence of peptides (Asp<sub>4</sub> or Gly-Asp), the amino acids are predominantly (>98%) incorporated as peptides, as opposed to free amino acids, and for the purposes of this discussion, we assume that both peptides are stable and not hydrolyzed during the experiments. The observations in the two series of experiments show that peptides and amino acids can influence aragonite formation in different ways. Both Asp and Asp<sub>4</sub> inhibit aragonite precipitation, but building aspartic acid into a tetra-peptide increases the inhibition of aragonite precipitation relative to the number of amino acid residues present; for example, the 1 mM Asp<sub>4</sub> and the 4 mM Asp treatments contain the same number of aspartic acid residues in solution, yet the aragonite precipitation rate in the Asp<sub>4</sub> treatment is ~20% of that in the Asp treatment (Figure 3b). Similar effects are reported for Asp monomers and polymers in calcite.<sup>16,17,50,51</sup> However, the Gly-Asp dipeptide has no greater effect on aragonite precipitation inhibition compared to Asp (Figure 3a and Table 1), indicating that the increase in molecule size in this case has no significant effect.

Amino acids and peptides affect CaCO<sub>3</sub> formation by binding the aqueous ions required for mineral formation,<sup>52</sup> by influencing the attachment of ions to an existing crystal surface,<sup>7</sup> or by affecting the formation of CaCO<sub>3</sub> precursor phases.<sup>12</sup> Little CaCO<sub>3</sub> formation is observed in unseeded

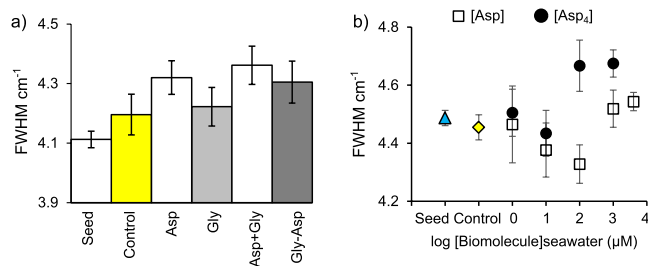


**Figure 5.** Raman  $\nu_1$  fwhm in synthetic aragonite in a) the 330 mL experiments with 2 mM amino acids and peptides and b) the 33 mL experiments with varying concentrations of Asp and Asp<sub>4</sub>. 12–15 spectra were collected for each precipitate, and at least two precipitates (from replicate titrations) were analyzed in each treatment (except for 1 mM Asp<sub>4</sub>, where only one precipitate was produced). Data from multiple replicate titrations were combined for analysis. Bars/points represent means ( $n = 16$ –50) and error bars show 1 standard deviation.

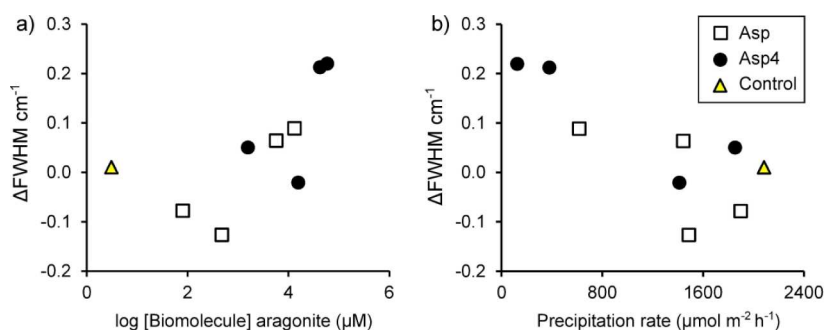


**Figure 6.**  $\Delta$ fwhm (deviation of fwhm in the sample from that of the control) as a function of a) seawater biomolecule concentration, b) aragonite amino acid concentration, and c) aragonite precipitation rate.

**Table 2. Coefficients of Determination ( $r^2$ ) and  $p$ -Values of Regression Analysis of Relationships between the  $\Delta$ FWHM and Biomolecule Concentration or Aragonite Precipitation Rate<sup>a</sup>**

	$\Delta$ fwhm vs seawater [biomolecule]		$\Delta$ fwhm vs aragonite [biomolecule]		$\Delta$ fwhm vs precipitation rate	
	$r^2$	$p$	$r^2$	$p$	$r^2$	$p$
Asp ( $n = 6$ )	0.11	0.52	0.11	0.51	0.20	0.37
Asp <sub>4</sub> ( $n = 5$ )	0.67	0.088	0.39	0.26	0.82	<b>0.033</b>
all experiments combined ( $n = 10$ )	0.17	0.24	0.35	0.069	0.60	$8.7 \times 10^{-3}$

<sup>a</sup> $p$ -values  $\leq 0.05$  are highlighted in bold.

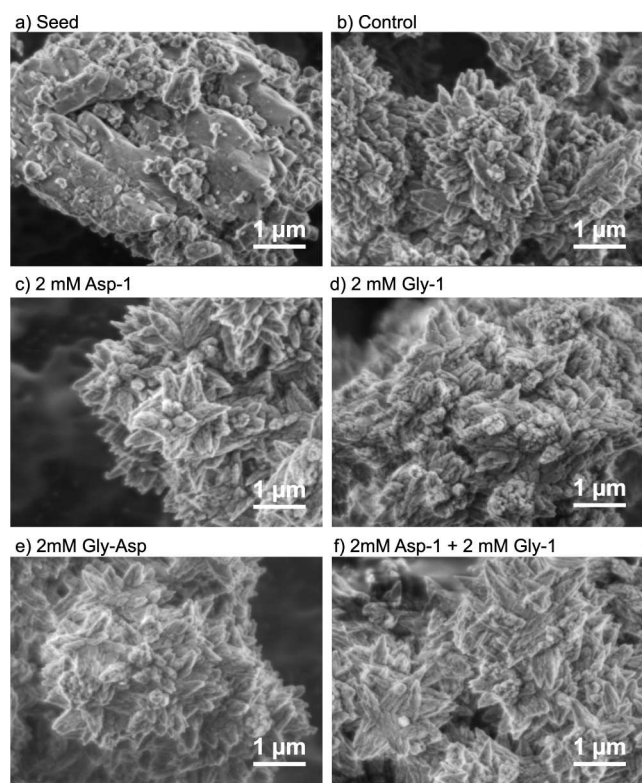


**Figure 7.** Scanning electron microscopy images of a) the coral seed and of aragonite precipitated in the 330 mL experiments: b) without biomolecule, c) with 2 mM Asp, d) with 2 mM Gly, e) with 2 mM Gly-Asp, and f) 2 mM Asp + 2 mM Gly.

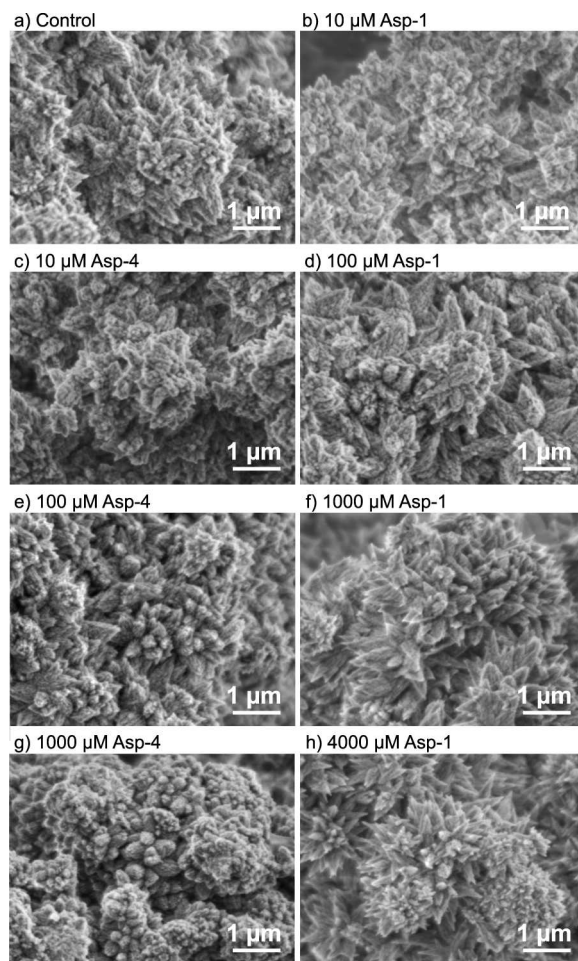


**Figure 8.** Scanning electron microscopy images of aragonite precipitated in the 33 mL experiments with a) no biomolecule, b), d), f), and h) with 10, 100, 1000, and 4000  $\mu$ M Asp respectively, and c), e), and g) with 10, 100, and 1000  $\mu$ M Asp<sub>4</sub>, respectively.

experiments under the conditions of the present study, indicating that precipitation proceeds in the presence of an existing aragonite surface, i.e., the seed.<sup>18</sup> In the present study, we observe incorporation of the amino acids and peptides into the intracrystalline fraction of the aragonite, indicating an interaction with the solid or a precursor phase. At pH 8.4, both Asp and Gly have a protonated amine group,  $\text{NH}_3^+$ , and a deprotonated  $\alpha$ -carboxylate group,  $\text{COO}^-$ .<sup>31</sup> In calcite, deprotonated amino acid carboxyl groups ( $\text{COO}^-$ ) may attract to  $\text{Ca}^{2+}$  sites while protonated amine groups ( $\text{NH}_3^+$ ) may

interact with  $\text{CO}_3^{2-}$  sites.<sup>17</sup> In addition, the acidic side chain(s) of Asp (and we assume of  $\text{Asp}_4$ ) are deprotonated at physiological pH and above.<sup>53</sup> This implies that all of the biomolecules used in this study can develop electrostatic interactions with the existing crystal surface. Once associated with the crystal surface, additives can inhibit  $\text{CaCO}_3$  growth by blocking ion attachment sites,<sup>54,55</sup> may become entrapped in the crystal by progressive  $\text{CaCO}_3$  growth around the additive<sup>55,56</sup> or may remain at the crystal surface and not be incorporated as the  $\text{CaCO}_3$  grows.<sup>55</sup>

The aragonite [Asp] and [Gly] in the present study are much lower than reported in previous studies of calcite<sup>57,58</sup> where  $[\text{Asp}]_{\text{calcite}}$  and  $[\text{Gly}]_{\text{calcite}}$  reached up to  $\sim 4$  mol % and  $\sim 7$  mol %, respectively (equivalent to  $\sim 400$  nmol  $\text{mg}^{-1}$  and  $\sim 700$  nmol  $\text{mg}^{-1}$ , respectively).  $[\text{Amino acid}]_{\text{calcite}}$  is positively related to  $[\text{amino acid}]_{\text{solution}}$ <sup>58</sup> and in these previous studies, calcite was precipitated at higher [amino acid]<sub>solution</sub> than used in the present study.<sup>57,58</sup> In addition,  $[\text{Asp}]_{\text{calcite}}$  and  $[\text{Gly}]_{\text{calcite}}$  vary considerably between precipitations with comparable  $[\text{amino acid}]_{\text{solution}}$  in these previous studies, highlighting the importance of other experimental conditions in amino acid incorporation.

In our study,  $\text{Asp}_4$  is incorporated more effectively than Asp at comparable solution concentrations (Figure 4b), even assuming that each  $\text{Asp}_4$  molecule contributes 4 aspartic acid residues to the aragonite [Asp]. Asp is incorporated more effectively than Gly (Figure 4a). This likely reflects the strength of interactions between the biomolecule and the growing crystal surface. At the study pH,  $\text{Asp}_4$  has a higher negative charge ( $-4$ ) than Asp ( $-1$ ), which is itself more charged than the uncharged but polar Gly. Similarly, in calcite, both Asp and Gly and their mono-peptides adsorb to the mineral surface, and Asp polymers adsorb more strongly than Asp.<sup>17</sup>

We precipitate aragonite over variable concentrations of Asp and  $\text{Asp}_4$ , and we observe different relationships between seawater and aragonite concentrations in each case. In the Asp experiments, incorporation of Asp in the aragonite had little effect on seawater [Asp] ( $<1\%$ ) and aragonite [Asp] is proportional to seawater [Asp] over the entire analyzed range (1–2000  $\mu\text{M}$ , Figure 4c). This suggests that adsorption sites of the amino acid onto the aragonite are not saturated during the precipitation. In contrast, in the  $\text{Asp}_4$  experiments, aragonite [Asp] flattens out at high seawater  $[\text{Asp}_4]$  (Figure 4b), indicating that adsorption sites are becoming saturated as seawater  $[\text{Asp}_4]$  increases. We estimate that the incorporation of  $\text{Asp}_4$  into the aragonite reduces the seawater  $[\text{Asp}_4]$  by  $\sim 10\%$  at the highest seawater  $\text{Asp}_4$  and we consider this to be a small reduction. In the highest  $[\text{Asp}_4]$  tested, aragonite [Asp] reaches 58 nmol  $\text{mg}^{-1}$ , indicating that  $\text{Asp}_4$  and  $\text{CaCO}_3$  occur in the solid phase in a molar ratio of 1:690 (assuming that the incorporation of 1 nmol of  $\text{Asp}_4$  increases aragonite [Asp] by 4 nmol and that  $\text{CaCO}_3$  has a molecular mass of 100 g). In this experiment, the aragonite precipitation rate is reduced by  $>93\%$ , suggesting that the incorporation of the biomolecule in this ratio severely suppresses crystal growth.

To explore the relationship between biomolecule incorporation in aragonite and growth rate, we plot the aragonite precipitation rate as a function of aragonite [Asp] for the experiments conducted over varying seawater [Asp] and  $[\text{Asp}_4]$  (Figure 9). Both  $\text{Asp}_4$  and Asp show significant inverse relationships between aragonite [Asp] and precipitation rate ( $p = 3.8 \times 10^{-5}$  and 0.038 respectively), but the coefficient of

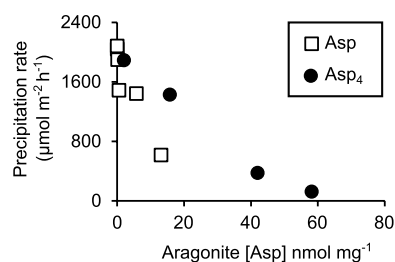


**Figure 9.** Aragonite precipitation rate as a function of aragonite [Asp] in the precipitations in the presence of Asp and  $\text{Asp}_4$ .

determination ( $r^2$ ) is much higher for  $\text{Asp}_4$  (0.97) than for Asp (0.61). This is potentially because the low [Asp] tested here has little effect on the aragonite precipitation rate or on aragonite Asp incorporation. However, it is notable that similar aragonite precipitation rates ( $\sim 1400$ – $1500$   $\mu\text{mol m}^{-2} \text{h}^{-1}$ ) are associated with aragonite [Asp] of  $<7$  nmol  $\text{mg}^{-1}$  in aragonite precipitated in the presence of Asp, but with aragonite [Asp] of  $<12$  nmol  $\text{mg}^{-1}$  in aragonite precipitated with  $\text{Asp}_4$ . Put another way, our study indicates that each aspartic acid residue incorporated into the aragonite suppresses aragonite precipitation more in the free amino acid than in the peptide form. Potentially, this reflects the number of ion attachment sites that are blocked by each molecule, e.g., four free aspartic acid residues can potentially block 4 sites while a single  $\text{Asp}_4$  molecule may only be able to block 1 site. To summarize, the comparison of Asp and  $\text{Asp}_4$  indicates that  $\text{Asp}_4$  inhibits aragonite precipitation more than Asp at comparable solution concentrations (Figure 3) but that Asp reduces aragonite precipitation more effectively than  $\text{Asp}_4$  for each Asp residue incorporated into the aragonite (Figure 9).

Asp has markedly different effects on aragonite morphology compared to those of  $\text{Asp}_4$ . In the presence of Asp, the pyramidal aragonite crystals become pointier (Figure 8h), while in the presence of  $\text{Asp}_4$ , they become shorter and stubbier (Figure 8g). This indicates that the two biomolecules interact with the aragonite growth surface in different ways. Additives may alter calcite crystal morphology by adsorbing preferentially to particular faces,<sup>59</sup> thereby promoting the development of other faces where the adsorbent is absent,<sup>50,60,61</sup>

In the present study, both the Gly-Asp dipeptide and free Asp have similar effects on the aragonite precipitation rate (Figure 3) and result in similar aragonite [Asp] (Figure 4a). Aragonite precipitated with this dipeptide has higher [Gly] compared to aragonite precipitated with only Gly or with both Asp and Gly in free amino acid form. This suggests that the incorporation of the dipeptide in aragonite is driven principally by the interaction of the Asp residue with the crystal surface and that the Gly residue has no discernible role, either in terms of its own chemistry or because it increases the size of the biomolecule. Gly has little impact on the aragonite precipitation rate when included as a single amino acid in isolation (Figure 3a).

Low concentrations of amino acids and peptides promote  $\text{CaCO}_3$  growth in calcite,<sup>16,17,50</sup> For crystal growth from aqueous  $\text{Ca}^{2+}$  and  $\text{CO}_3^{2-}$ , the rate-limiting step is the desolvation of  $\text{Ca}^{2+}$  prior to binding to the crystal surface.<sup>62</sup> Low concentrations of amino acids and peptides promote desolvation and decrease the energy barrier to the attachment of ions at the crystal surface.<sup>16</sup> Low concentrations of aspartic acid (1 and 10  $\mu\text{M}$ ) accelerated aragonite precipitation in

artificial seawater<sup>18</sup> but this effect is less clear in the present study (Figure 3b). Here, varying [Asp] was tested in small volume experiments (33 mL) for direct comparison with the Asp<sub>4</sub> data. We observe large variations between replicate titrations in these small volume experiments (coefficient of variation of up to 32%, Figure 3b) compared to the large volume experiments undertaken by Kellock et al.<sup>18</sup> (coefficient of variation < 9%). This may reflect heterogeneity in the surface area of the seed used in the experiments. Seeds were produced by wet grinding a coral skeleton<sup>18</sup> or a synthetic aragonite (33 mL experiments in the present study), resulting in irregular particles (e.g., Figure 7a). Variations in seed surface area will have more obvious effects on aragonite precipitation rate in the small volume experiments, which used a smaller seed mass (20 mg) compared to the large volume analogues (200 mg). Similarly, 2 mM Gly significantly reduced aragonite precipitation rate in a previous study in our laboratory<sup>53</sup> but the effect was small (~16% at pH<sub>NBS</sub> 8.445 and  $\Omega_{\text{aragonite}} \approx 12.5$ ), and this effect is not observed in the present study. The coefficient of variation of aragonite precipitation rates in replicate precipitations is up to 10% in the 330 mL experiments in the present study, so a small reduction or increase in precipitation rate is difficult to resolve without a larger number of experiments.<sup>63</sup>

Aragonite precipitation rates in the control experiments conducted at  $\Omega = 11$  varied from  $\sim 3500 \mu\text{mol h}^{-1} \text{m}^{-2}$  in the experiments using the coral skeleton as a seed to  $\sim 2040 \mu\text{mol h}^{-1} \text{m}^{-2}$  in the experiments using the synthetic aragonite seed (Figure 3). The origin of this difference is unclear. Potentially, the biomolecule content of the coral skeleton seed alters nucleation and accelerates aragonite precipitation.

**4.2. Biomolecules and Aragonite Structure.** High concentrations of all biomolecules, except glycine, increased the Raman spectrum  $\nu_1$  band fwhm, interpreted as indicative of CO<sub>3</sub> rotational disorder<sup>33</sup> (Figure 5 and Table 1). All of the amino acids and peptides tested here are incorporated into the aragonite structure. Unit cell volume and Raman  $\nu_1$  band fwhm were positively correlated across synthetic and biogenic aragonites<sup>64</sup> and the inclusion of Asp and Gly expanded the *a* and *c* lattice parameters of calcite precipitated at ambient laboratory temperature,<sup>57,58</sup> although the incorporation of Asp decreased the lattice parameter in calcite precipitated at 134 °C.<sup>65</sup> Lattice distortions are also observed in mollusk aragonite<sup>66</sup> and calcite<sup>67</sup> and in coral aragonite<sup>64</sup> compared to geological minerals. The origin of these effects is not clear. Aspartic acid molecules have dimensions of 4–7 Å based on the bond length and angle<sup>68</sup> while the unit cell of aragonite is  $\sim 5 \times 8 \times 6$  Å.<sup>69</sup> Adsorbed molecules can become entrapped in the mineral lattice if they are buried in the crystal structure by subsequent mineral growth before desorption occurs.<sup>55,56</sup> The biomolecules entrapped in aragonite in the present study may modify the local environment around the CO<sub>3</sub> groups, thereby creating the disorder. We do not observe significant relationships between aragonite [Asp] and the shift in the aragonite fwhm from that observed in the control ( $\Delta\text{fwhm}$ , Figure 6a and Table 2). However, the numbers of analyses are small and little Asp is incorporated into aragonite at low [Asp], so it is difficult to resolve a relationship. We do observe a significant inverse relationship between the change in the fwhm of precipitates with Asp and Asp<sub>4</sub> compared to that of the controls and aragonite precipitation rate for all of our synthetic precipitates (Figure 6b), indicating that there is a link between growth rate and aragonite crystallinity.

Besides biomolecule incorporation, CO<sub>3</sub> rotational disorder may also reflect distortion of the CaCO<sub>3</sub> lattice structure dependent on the incorporation of other impurity ions in the aragonite lattice.<sup>64</sup> CaCO<sub>3</sub> biominerals are impure and contain a variety of cations (e.g., Sr<sup>2+</sup>, Mg<sup>2+</sup>, Na<sup>+</sup>) and anions (e.g., B(OH)<sub>4</sub><sup>-</sup>) which either substitute into the crystal lattice, e.g., Sr<sup>2+</sup> replaces Ca<sup>2+</sup> in aragonite<sup>36</sup> or are incorporated by other means, as for Mg<sup>2+</sup> in aragonite.<sup>70</sup> Substitution of impurity ions causes dilation or contraction of the site and creates strain in the lattice.<sup>71</sup> Fast mineral growth rates may enhance impurity ion incorporation if the impurities attach to the crystal surface and then become entrapped by rapid precipitation before they can detach,<sup>72</sup> and indeed, the Raman spectrum  $\nu_1$  fwhm has been used as a metric of Mg/Ca in calcite.<sup>73</sup> The inverse relationship between aragonite precipitation rate and Raman spectrum  $\nu_1$  band fwhm observed in the present study is contrary to a previous report where increased disorder was observed in aragonite precipitated with no additives at higher  $\Omega_{\text{aragonite}}$  when mineral precipitation rates were rapid.<sup>48</sup> Further work is required to identify how biomolecules and fluid  $\Omega$  interact with mineral precipitation rate and impurity inclusion to affect the aragonite structure. Our observation that Gly-Asp has no greater effect on aragonite precipitation or  $\nu_1$  peak fwhm than free aspartic acid, suggests that molecules of this size have limited effects on mineral growth rate or structure.

The Raman  $\nu_1$  band fwhm is significantly narrower in aragonite precipitated with 10 and 100  $\mu\text{M}$  Asp than in the controls. Similar narrowing was not observed in aragonite precipitated under similar conditions in a prior study.<sup>18</sup> The fwhm of the control precipitated in the prior study ( $\sim 4.23 \text{ cm}^{-1}$ ) is considerably lower than that observed in the present study ( $4.45 \text{ cm}^{-1}$ ). This suggests that the Raman signature is influenced by the different seed materials used in each study (coral in Kellock et al, 2022<sup>18</sup> and synthetic aragonite in the present study). Narrowing of the fwhm at low [Asp] may not have been apparent in the prior study, as the fwhm of the aragonite produced in the presence of 10 and 100  $\mu\text{M}$  Asp in the present study (Figure 5) appears to be close to the fwhm of the seed used in Kellock et al, 2022.<sup>18</sup>

**4.3. Implications for Biomineralization.** Aspartic acid is the predominant amino acid in many coral skeletons,<sup>1,23</sup> is abundant in mollusk shells<sup>27–29</sup> and occurs in consecutive positions of coral acid-rich proteins, CARPs.<sup>30</sup> It is unclear precisely how proteins influence skeletal formation;<sup>23,25,74</sup> however, our study demonstrates that amino acids and peptides are incorporated into the aragonite. [Asp] in coral skeletons is measured as aspartic acid and asparagine combined (Asx) but is inferred to reflect predominantly Asp, as Asp:Arg is  $\sim 10:1$  in a coral acidic amino acid-rich skeletal protein.<sup>30</sup> [Asx] and [Gly] in cultured coral skeletons range from  $\sim 0.5$  to  $1.5 \text{ nmol mg}^{-1}$  and  $0.2$  to  $0.8 \text{ nmol mg}^{-1}$  respectively.<sup>23</sup> [Asx] and [Gly] in mollusk shells are up to  $1$  and  $2 \text{ nmol mg}^{-1}$  respectively.<sup>75</sup> The [Asp] and [Gly] in the synthetic aragonites in the present study range from  $0.07$  to  $58 \text{ nmol mg}^{-1}$  (Figure 4c,d) and  $1$  to  $16 \text{ nmol mg}^{-1}$  (Figure 4a), respectively, indicating that the aragonites produced here have comparable amino acid contents to aragonitic biominerals.

Our study shows that low solution concentrations ( $1 \mu\text{M}$ ) of Asp<sub>4</sub> reduce aragonite precipitation, suggesting that CARPs may inhibit biomineralization. Direct pH and CO<sub>3</sub><sup>2-</sup> measurements of the coral extracellular calcification media suggest the media has  $\Omega_{\text{aragonite}}$  of  $\approx 12$ .<sup>76</sup> At this  $\Omega$ , homogeneous

aragonite nucleation (in the absence of a nucleation surface) is not observed<sup>77</sup> but precipitation is rapid onto an existing aragonite surface,<sup>18,23,78</sup> as occurs when coral skeletal growth proceeds by ion-by-ion attachment onto the existing skeleton.<sup>9</sup> CARPs may therefore act to inhibit aragonite precipitation, to prevent uncontrolled formation of the mineral phase, and to shape the coral skeleton.

## 5. CONCLUSION

All biomolecules are incorporated into aragonite to produce solids with [amino acids] comparable to those of biogenic aragonite. Asp, Asp<sub>4</sub>, and Asp-Gly inhibit aragonite precipitation at the solution concentrations required to generate these solids, suggesting that aspartic acid acts to suppress (rather than accelerate) biomineral formation. Biomolecule-driven changes in crystal morphology are very different between Asp and Asp<sub>4</sub>, perhaps indicating the preferential binding of each biomolecule to different crystal faces. Asp<sub>4</sub> inhibits aragonite precipitation more than Asp at comparable solution concentrations, but Asp reduces aragonite precipitation more effectively than Asp<sub>4</sub> for each Asp residue incorporated into the aragonite, potentially reflecting the ability of each biomolecule to block binding sites for precipitation.

## ■ ASSOCIATED CONTENT

### SI Supporting Information

The Supporting Information is available free of charge at <https://pubs.acs.org/doi/10.1021/acs.cgd.4c00766>.

Further details of the method to confirm minimal CO<sub>2</sub> outgassing or invasion during titrations (the Method section and Figure S1); details of the HPLC solvent gradient (Table S1); all aragonite precipitation rates, aragonite [amino acid], and Raman  $\nu_1$  band fwhm (Tables S2–S6); example Raman spectra of aragonite and biomolecules (Figure S2) and the fwhm of the Raman  $\nu_1$  band in repeat analyses on the same location of aragonite with no biomolecule (control), Asp, and Asp<sub>4</sub> (Figure S3); lower magnification scanning electron micrographs of all precipitates (Figures S4 and S5) (PDF)

## ■ AUTHOR INFORMATION

### Corresponding Author

Nicola Allison – School of Earth and Environmental Sciences, University of St. Andrews, St Andrews KY16 9TS, U.K.; Scottish Oceans Institute, University of St. Andrews, St Andrews KY16 8LB, U.K.; [orcid.org/0000-0003-3720-1917](https://orcid.org/0000-0003-3720-1917); Email: [na9@st-andrews.ac.uk](mailto:na9@st-andrews.ac.uk)

### Authors

Giacomo Gardella – School of Earth and Environmental Sciences, University of St. Andrews, St Andrews KY16 9TS, U.K.; Scottish Oceans Institute, University of St. Andrews, St Andrews KY16 8LB, U.K.; [orcid.org/0009-0005-7209-9374](https://orcid.org/0009-0005-7209-9374)

Maria Cristina Castillo Alvarez – School of Earth and Environmental Sciences, University of St. Andrews, St Andrews KY16 9TS, U.K.; Scottish Oceans Institute, University of St. Andrews, St Andrews KY16 8LB, U.K.

Sam Presslee – Department of Chemistry, University of York, York YO10 5DD, U.K.

Adrian A. Finch – School of Earth and Environmental Sciences, University of St. Andrews, St Andrews KY16 9TS, U.K.

Kirsty Penkman – Department of Chemistry, University of York, York YO10 5DD, U.K.

Roland Kröger – Department of Physics, University of York, York YO10 5DD, U.K.

Matthieu Clog – SUERC, University of Glasgow, Glasgow G75 0QF, U.K.

Complete contact information is available at: <https://pubs.acs.org/10.1021/acs.cgd.4c00766>

## Notes

The authors declare no competing financial interest.

## ■ ACKNOWLEDGMENTS

This work was supported by the UK Natural Environment Research Council (NE/S001417/1) to NA, KP, RK, MC, and AF. We thank Gavin Peters, University of St Andrews, for assistance with BET analyses, and Adam Kerrigan and Sheila Taylor, University of York, for assistance with SEM and amino acid analysis, respectively. Raman analyses were supported by the EPSRC Light Element Analysis Facility Grant EP/T019298/1 and EPSRC Strategic Equipment Resource Grant EP/R023751/1 at the University of St Andrews. For the purpose of open access, the authors have applied a Creative Commons Attribution (CC BY) license to any Author Accepted Manuscript version arising from this submission.

## ■ REFERENCES

- (1) Cuif, J. P.; Dauphin, Y.; Freiwald, A.; Gautret, P.; Zibrowius, H. Biochemical Markers of Zooxanthellae Symbiosis in Soluble Matrices of Skeleton of 24 Scleractinia Species. *Comp. Biochem. Physiol. - A Mol. Integr. Physiol.* **1999**, *123*, 269–278.
- (2) Estroff, L. A. Introduction: Biomineralization. *Chem. Rev.* **2008**, *108*, 4329–4331.
- (3) Gebauer, D.; Cölfen, H.; Verch, A.; Antonietti, M. The Multiple Roles Of Additives in CaCO<sub>3</sub> Crystallization: A Quantitative Case Study. *Adv. Mater.* **2009**, *21*, 435–439.
- (4) Addadi, L.; Weiner, S. Interactions between Acidic Proteins and Crystals: Stereochemical Requirements In Biomineralization. *Proc. Nat. Acad. Sci.* **1985**, *82*, 4110–4114.
- (5) Gránásy, L.; Rátkai, L.; Tóth, G. I.; Gilbert, P. U.; Zlotnikov, I.; Pusztai, T. Phase-Field Modeling of Biomineralization in Mollusks and Corals: Microstructure vs Formation Mechanism. *JACS Au* **2021**, *1*, 1014–1033.
- (6) Ihli, J.; Clark, J. N.; Kanwal, N.; Kim, Y. Y.; Holden, M. A.; Harder, R. J.; Tang, C. C.; Ashbrook, S. E.; Robinson, I. K.; Meldrum, F. C. Visualization of the Effect of Additives on the Nanostructures of Individual Bio-Inspired Calcite Crystals. *Chem. Sci.* **2019**, *10*, 1176–1185.
- (7) De Yoreo, J. J.; Vekilov, P. G. Principles of Crystal Nucleation and Growth. *Rev. Mineral Geochem.* **2003**, *54*, 57–93.
- (8) De Yoreo, J. J.; Gilbert, P. U. P. A.; Sommerdijk, N. A. J. M.; Penn, R. L.; Whitelam, S.; Joester, D.; Zhang, H.; Rimer, J. D.; Navrotsky, A.; Banfield, J. F.; et al. Crystallization by Particle Attachment in Synthetic, Biogenic, and Geologic Environments. *Science* **2015**, *349* (6247), aaa6760.
- (9) Sun, C. Y.; Marcus, M. A.; Frazier, M. J.; Giuffrè, A. J.; Mass, T.; Gilbert, P. U. P. A. Spherulitic Growth of Coral Skeletons and Synthetic Aragonite: Nature's Three-Dimensional Printing. *ACS Nano* **2017**, *11*, 6612–6622.
- (10) De Stefano, C.; Foti, C.; Gianguzza, A.; Rigano, C.; Sammartano, S. Chemical Speciation of Amino Acids in Electrolyte

Solutions Containing Major Components of Natural Fluids. *Chem. Speciat. Bioavailab.* **1995**, *7*, 1–8.

(11) Politi, Y.; Mahamid, J.; Goldberg, H.; Weiner, S.; Addadi, L. Asprich Mollusk Shell Protein: *In Vitro* Experiments Aimed at Elucidating Function In CaCO<sub>3</sub> Crystallization. *CrystEngcomm* **2007**, *9*, 1171–1177.

(12) Kellermeier, M.; Gebauer, D.; Melero-García, E.; Drechsler, M.; Talmon, Y.; Kienle, L.; Cölfen, H.; García-Ruiz, J. M.; Kunz, W. Colloidal Stabilization of Calcium Carbonate Prenucleation Clusters With Silica. *Adv. Funct. Mater.* **2012**, *22*, 4301–4311.

(13) Jiang, W.; Athanasiadou, D.; Zhang, S.; Demichelis, R.; Koziara, K. B.; Raiteri, P.; Nelea, V.; Mi, W.; Ma, J. A.; Gale, J. D.; et al. Homochirality in Biomineral Suprastructures Induced by Assembly of Single-Enantiomer Amino Acids from a Nonracemic Mixture. *Nat. Commun.* **2019**, *10* (1), 2318.

(14) Picker, A.; Kellermeier, M.; Seto, J.; Gebauer, D.; Cölfen, H. The Multiple Effects of Amino Acids on the Early Stages of Calcium Carbonate Crystallization. *Z. Kristallogr. - Cryst. Mater.* **2012**, *227*, 744–757.

(15) Tong, H.; Ma, W.; Wang, L.; Wan, P.; Hu, J.; Cao, L. Control Over the Crystal Phase, Shape, Size and Aggregation of Calcium Carbonate Via a L-Aspartic Acid Inducing Process. *Biomaterials* **2004**, *25*, 3923–3929.

(16) Elhadj, S.; De Yoreo, J. J.; Hoyer, J. R.; Dove, P. M. Role of Molecular Charge and Hydrophilicity in Regulating the Kinetics of Crystal Growth. *Proc. Nat. Acad. Sci.* **2006**, *103*, 19237–19242.

(17) Montanari, G.; Lakshtanov, L. Z.; Tobler, D. J.; Dideriksen, K.; Dalby, K. N.; Bovet, N.; Stipp, S. L. S. Effect of Aspartic Acid and Glycine on Calcite Growth. *Cryst. Growth Des.* **2016**, *16*, 4813–4821.

(18) Kellock, C.; Castillo Alvarez, M. C.; Finch, A.; Penkman, K.; Kröger, R.; Clog, M.; Allison, N. Optimising a Method for Aragonite Precipitation in Simulated Biogenic Calcification Media. *PLoS One* **2022**, *17*, No. e0278627.

(19) Vinn, O. Biomineralization in Polychaete Annelids: A review. *Minerals* **2021**, *11*, 1151.

(20) Bandy, O. L. Aragonite Tests Among Foraminifera. *J. Sediment. Res.* **1954**, *24*, 60–61.

(21) Grégoire, C. Structure of the Molluscan Shell. *Chem. Zool.* **1972**, *7*, 45–102.

(22) Wainwright, S. A. Skeletal Organization in the Coral, *Pocillopora damicornis*. *J. Cell Sci* **1963**, *s3-104*, 169–183.

(23) Kellock, C.; Cole, C.; Penkman, K.; Evans, D.; Kröger, R.; Hintz, C.; Hintz, K.; Finch, A.; Allison, N. The Role of Aspartic Acid in Reducing Coral Calcification Under Ocean Acidification Conditions. *Sci. Rep.* **2020**, *10* (1), 12797.

(24) Nahi, O.; Kulak, A. N.; Zhang, S.; He, X.; Aslam, Z.; Ilett, M. A.; Ford, I. J.; Darkins, R.; Meldrum, F. C. Polyamines Promote Aragonite Nucleation and Generate Biomimetic Structures. *Adv. Sci.* **2023**, *10* (1), 2203759.

(25) Tambutté, E.; Venn, A. A.; Holcomb, M.; Segonds, N.; Techer, N.; Zoccola, D.; Allemand, D.; Tambutté, S. Morphological Plasticity of the Coral Skeleton Under CO<sub>2</sub>-Driven Seawater Acidification. *Nat. Commun.* **2015**, *6*, 7368.

(26) Coronado, I.; Fine, M.; Bosellini, F. R.; Stolarski, J. Impact of Ocean Acidification on Crystallographic Vital Effect of the Coral Skeleton. *Nat. Commun.* **2019**, *10* (1), 2896.

(27) Weiner, S. Aspartic Acid-Rich Proteins: Major Components of the Soluble Organic Matrix of Mollusk Shells. *Calcif. Tissue Int.* **1979**, *29*, 163–167.

(28) Bédouet, L.; Schuller, M. J.; Marin, F.; Milet, C.; Lopez, E.; Giraud, M. Soluble Proteins of The Nacre of the Giant Oyster *Pinctada maxima* and of the Abalone *Haliotis tuberculata*: Extraction and Partial Analysis of Nacre Proteins. *Comp. Biochem. Physiol. B Biochem. Mol. Biol.* **2001**, *128* (3), 389–400.

(29) Suzuki, M.; Saruwatari, K.; Kogure, T.; Yamamoto, Y.; Nishimura, T.; Kato, T.; Nagasawa, H. An Acidic Matrix Protein, Pif, is a Key Macromolecule for Nacre Formation. *Science* **2009**, *325*, 1388–1390.

(30) Mass, T.; Drake, J. L.; Haramaty, L.; Kim, J. D.; Zelzion, E.; Bhattacharya, D.; Falkowski, P. G. Cloning and Characterization of Four Novel Coral Acid-Rich Proteins That Precipitate Carbonates *In Vitro*. *Curr. Biol.* **2013**, *23*, 1126–1131.

(31) Lide, D. R. *CRC Handbook of Chemistry and Physics*; CRC press, 2004; Vol. 85.

(32) Tang, N.; Skibsted, L. H. Calcium binding to Amino Acids and Small Glycine Peptides in Aqueous Solution: Toward Peptide Design for Better Calcium Bioavailability. *J. Agric. Food Chem.* **2016**, *64*, 4376–4389.

(33) Bischoff, W. D.; Sharma, S. K.; MacKenzie, F. T. Carbonate Ion Disorder in Synthetic and Biogenic Magnesian Calcites: A Raman Spectral Study. *Am. Mineral.* **1985**, *70*, 581–589.

(34) DeCarlo, T. M.; D'Olivo, J. P.; Foster, T.; Holcomb, M.; Becker, T.; McCulloch, M. T. Coral Calcifying Fluid Aragonite Saturation States Derived from Raman Spectroscopy. *Biogeosciences* **2017**, *14*, 5253–5269.

(35) Beck, R.; Seiersten, M.; Andreassen, J. P. The Constant Composition Method for Crystallization of Calcium Carbonate at Constant Supersaturation. *J. Cryst. Growth* **2013**, *380*, 187–196.

(36) Finch, A. A.; Allison, N.; Sutton, S. R.; Newville, M. Strontium in Coral Aragonite: 1. Characterization of Sr Coordination by Extended Absorption X-ray Fine Structure. *Geochim. Cosmochim. Acta* **2003**, *67*, 1197–1202.

(37) Millero, F. J. *Chemical Oceanography*; CRC Press, 2013.

(38) Pierrot, D.; Lewis, E. D.; Wallace, W. R. *MS Excel Program Developed for CO<sub>2</sub>, System Calculations*; Oak Ridge National Laboratory, 2006.

(39) Lueker, T. J.; Dickson, A. G.; Keeling, C. D. Ocean pCO<sub>2</sub> Calculated from Dissolved Inorganic Carbon, Alkalinity, and Equations for K<sub>1</sub> and K<sub>2</sub>: Validation Based on Laboratory Measurements of CO<sub>2</sub> in Gas and Seawater at Equilibrium. *Mar. Chem.* **2000**, *70*, 105–119.

(40) Dickson, A. G. Standard Potential of the Reaction: AgCl(s) + 1/2H<sub>2</sub>(g) = Ag(s) + HCl(aq), and the Standard Acidity Constant of The Ion HSO<sub>4</sub><sup>-</sup> in Synthetic Sea Water from 273.15 to 318.15 K. *J. Chem. Thermodyn.* **1990**, *22*, 113–127.

(41) Lee, K.; Kim, T. W.; Byrne, R. H.; Millero, F. J.; Feely, R. A.; Liu, Y. M. The Universal Ratio of Boron to Chlorinity for the North Pacific and North Atlantic Oceans. *Geochim. Cosmochim. Acta* **2010**, *74*, 1801–1811.

(42) Brunauer, S.; Emmett, P. H.; Teller, E. Adsorption of Gases in Multimolecular Layers. *J. Am. Chem. Soc.* **1938**, *60*, 309–319.

(43) Cole, C.; Finch, A.; Hintz, C.; Hintz, K.; Allison, N. Understanding Cold Bias: Variable Response of Skeletal Sr/Ca to Seawater pCO<sub>2</sub> in Acclimated Massive *Porites* Corals. *Sci. Rep.* **2016**, *6* (1), 26888.

(44) Hendy, E. J.; Tomiak, P. J.; Collins, M. J.; Hellstrom, J.; Tudhope, A. W.; Lough, J. M.; Penkman, K. E. Assessing Amino Acid Racemization Variability in Coral Intra-Crystalline Protein for Geochronological Applications. *Geochim. Cosmochim. Acta* **2012**, *86*, 338–353.

(45) Kaufman, D. S.; Manley, W. F. A New Procedure for Determining DL Amino Acid Ratios in Fossils Using Reverse Phase Liquid Chromatography. *Quat. Sci. Rev.* **1998**, *17*, 987–1000.

(46) Nasdala, L.; Wenzel, M.; Vavra, G.; Irmer, G.; Wenzel, T.; Kober, B. Metamictisation of Natural Zircon: Accumulation Versus Thermal Annealing of Radioactivity-Induced Damage. *Contrib. Mineral. Petrol.* **2001**, *141*, 125–144.

(47) Hernández, B.; Pflüger, F.; Kruglik, S. G.; Ghomi, M. Protonation–Deprotonation of the Glycine Backbone as Followed by Raman Scattering and Multiconformational Analysis. *Chem. Phys.* **2013**, *425*, 104–113.

(48) DeCarlo, T. M. Characterizing Coral Skeleton Mineralogy with Raman Spectroscopy. *Nat. Commun.* **2018**, *9* (1), 5325.

(49) Urmos, J.; Mackenzie, F. T.; Sharma, S. K. Characterizations of Some Biogenic Carbonates with Raman Spectroscopy. *Am. Mineral* **1991**, *76*, 641–646.

- (50) Elhadj, S.; Salter, E. A.; Wierzbicki, A.; De Yoreo, J. J.; Han, N.; Dove, P. M. Peptide Controls on Calcite Mineralization: Polyaspartate Chain Length Affects Growth Kinetics and Acts as a Stereochemical Switch on Morphology. *Cryst. Growth Des.* **2006**, *6*, 197–201.
- (51) Njegic-Dzakula, B.; Brecevic, L.; Falini, G.; Kralj, D. Calcite Crystal Growth Kinetics in The Presence Of Charged Synthetic Polypeptides. *Cryst. Growth Des.* **2009**, *9*, 2425–2434.
- (52) Schuitemaker, A.; Koziara, K.; Raiteri, P.; Gale, J.; Demichelis, R. New Model for Aspartic Acid Species in Aqueous Calcium Carbonate Growth Environments: Challenges and Perspectives. *Phys. Chem. Chem. Phys.* **2024**, *26*, 4909–4921.
- (53) Voet, D.; Voet, J. G.; Pratt, C. W. *Fundamentals of Biochemistry: life at The Molecular Level*; John Wiley & Sons, 2016.
- (54) Sikirić, M. D.; Füredi-Milhofer, H. The Influence of Surface Active Molecules on the Crystallization of Biominerals in Solution. *Adv. Colloid Interface Sci.* **2006**, *128*, 135–158.
- (55) Cho, K. R.; Kulshreshtha, P.; Wu, K. J. J.; Seto, J.; Qiu, S. R.; De Yoreo, J. J. The Effects of Different Types Of Additives on Growth of Biomineral Phases Investigated by In Situ Atomic Force Microscopy. *J. Cryst. Growth* **2019**, *509*, 8–16.
- (56) Cho, K. R.; Kim, Y. Y.; Yang, P.; Cai, W.; Pan, H.; Kulak, A. N.; Lau, J. L.; Kulshreshtha, P.; Armes, S. P.; Meldrum, F. C.; et al. Direct observation of mineral–organic composite formation reveals occlusion mechanism. *Nat. Commun.* **2016**, *7* (1), 10187.
- (57) Borukhin, S.; Bloch, L.; Radlauer, T.; Hill, A. H.; Fitch, A. N.; Pokroy, B. Screening the Incorporation of Amino Acids into an Inorganic Crystalline Host: The Case of Calcite. *Adv. Funct. Mater.* **2012**, *22*, 4216–4224.
- (58) Kim, Y. Y.; Carloni, J. D.; Demarchi, B.; Sparks, D.; Reid, D. G.; Kunitake, M. E.; Tang, C. C.; Duer, M. J.; Freeman, C. L.; Pokroy, B.; Penkman, K.; Harding, J. H.; Estroff, L. A.; Baker, S. P.; Meldrum, F. C. Tuning Hardness in Calcite by Incorporation of Amino Acids. *Nat. Mater.* **2016**, *15*, 903–910.
- (59) Nada, H. Difference in the Conformation and Dynamics of Aspartic Acid on The Flat Regions, Step Edges, and Kinks of a Calcite Surface: A Molecular Dynamics Study. *J. Phys. Chem. C* **2014**, *118*, 14335–14345.
- (60) Teng, H. H.; Dove, P. M.; Orme, C. A.; De Yoreo, J. J. Thermodynamics of Calcite Growth: Baseline for Understanding Biomineral Formation. *Science* **1998**, *282*, 724–727.
- (61) Orme, C. A.; Noy, A.; Wierzbicki, A.; McBride, M. T.; Grantham, M.; Teng, H. H.; Dove, P. M.; De Yoreo, J. J. Formation of Chiral Morphologies Through Selective Binding of Amino Acids to Calcite Surface Steps. *Nature* **2001**, *411*, 775–779.
- (62) Nielsen, A. E. Electrolyte Crystal Growth Mechanisms. *J. Crystal Growth* **1984**, *67*, 289–310.
- (63) Castillo Alvarez, M. C.; Penkman, K.; Kröger, R.; Finch, A. A.; Clog, M.; Brasier, A.; Still, J.; Allison, N. Insights into the Response of Coral Biomineralisation to Environmental Change From Aragonite Precipitations In Vitro. *Geochim. Cosmochim. Acta* **2024**, *364*, 184–94.
- (64) Farfan, G. A.; Apprill, A.; Cohen, A.; DeCarlo, T. M.; Post, J. E.; Waller, R. G.; Hansel, C. M. Crystallographic and Chemical Signatures in Coral Skeletal Aragonite. *Coral Reefs* **2022**, *41*, 19–34.
- (65) Mijowska, S.; Polishchuk, I.; Lang, A.; Seknazi, E.; Dejoie, C.; Fermani, S.; Falini, G.; Demitri, N.; Polentarutti, M.; Katsman, A.; Pokroy, B. High Amino Acid Lattice Loading at Nonambient Conditions Causes Changes in Structure and Expansion Coefficient of Calcite. *Chem. Mater.* **2020**, *32*, 4205–4212.
- (66) Pokroy, B.; Quintana, J. P.; Caspi, E. A. N.; Berner, A.; Zolotoyabko, E. Anisotropic Lattice Distortions in Biogenic Aragonite. *Nat. Mater.* **2004**, *3*, 900–902.
- (67) Pokroy, B.; Fitch, A. N.; Marin, F.; Kapon, M.; Adir, N.; Zolotoyabko, E. Anisotropic Lattice Distortions in Biogenic Calcite Induced by Intra-Crystalline Organic Molecules. *J. Struct. Biol.* **2006**, *155*, 96–103.
- (68) Ching, C. B.; Hidajat, K.; Uddin, M. S. Evaluation of Equilibrium and Kinetic Parameters of Smaller Molecular Size Amino Acids on KX Zeolite Crystals Via Liquid Chromatographic Techniques. *Sep. Sci. Technol.* **1989**, *24*, 581–597.
- (69) De Villiers, J. P. R. Crystal Structures of Aragonite, Strontianite and Witherite. *Am. Mineral.* **1971**, *56*, 758–767.
- (70) Finch, A. A.; Allison, N. Mg Structural State in Coral Aragonite and Implications for the Paleoenvironmental Proxy. *Geophys. Res. Lett.* **2008**, *35* (8), L08704.
- (71) Finch, A. A.; Allison, N. Coordination of Sr and Mg in Calcite and Aragonite. *Mineral. Mag.* **2007**, *71*, 539–552.
- (72) Watson, E. A Conceptual Model for Near-Surface Kinetic Controls on the Trace-Element and Stable Isotope Composition of Abiogenic Calcite Crystals. *Geochim. Cosmochim. Acta* **2004**, *68*, 1473–1488.
- (73) Kamenos, N. A.; Burdett, H. L.; Aloisio, E.; Findlay, H. S.; Martin, S.; Longbone, C.; Dunn, J.; Widdicombe, S.; Calosi, P. Coralline Algal Structure is More Sensitive to Rate, Rather Than the Magnitude, of Ocean Acidification. *Global Change Biol.* **2013**, *19*, 3621–3628.
- (74) Falini, G.; Reggi, M.; Fermani, S.; Sparla, F.; Goffredo, S.; Dubinsky, Z.; Levi, O.; Dauphin, Y.; Cuif, J.-. Control of Aragonite Deposition in Colonial Corals by Intra-Skeletal Macromolecules. *J. Struct. Biol.* **2013**, *183*, 226–238.
- (75) Penkman, K. E. H.; Kaufman, D. S.; Maddy, D.; Collins, M. J. Closed-System Behaviour of the Intra-Crystalline Fraction of Amino Acids in Mollusc Shells. *Quat. Geochronol.* **2008**, *3*, 2–25.
- (76) Sevilgen, D. S.; Venn, A. A.; Hu, M. Y.; Tambutté, E.; de Beer, D.; Planas-Bielsa, V.; Tambutté, S. Full in Vivo Characterization of Carbonate Chemistry at the Site of Calcification in Corals. *Sci. Adv.* **2019**, *5* (1), No. eaau7447.
- (77) Morse, J. W.; He, S. Influences of T, S and pCO<sub>2</sub> on the Pseudo-Homogeneous Precipitation of CaCO<sub>3</sub> from Seawater: Implications for Whiting Formation. *Mar. Chem.* **1993**, *41*, 291–297.
- (78) Burton, E. A.; Walter, L. M. Relative Precipitation Rates of Aragonite and Mg Calcite from Seawater: Temperature or Carbonate Ion Control? *Geology* **1987**, *15*, 111–114.